25th International Symposium on Transportation and Traffic Theory, ISTTT 25, 15-17 July 2024
Ann Arbor, Michigan, United States

On Dynamic Fundamental Diagrams: Implications for Automated Vehicles

Jiwan Jiang[a], Yang Zhou[b], Xin Wang[c,*], and Soyoung (Sue) Ahn[a,*]

[a]*Department of Civil and Environmental Engineering, University of Wisconsin-Madison, Madison, WI 53706, USA*

[b]*Zachry Department of Civil and Environmental Engineering, Texas A&M University, College Station, TX 77843, USA*

[c]*Department of Industrial and Systems Engineering, University of Wisconsin-Madison, Madison, WI 53706, USA*

Abstract

The traffic fundamental diagram (FD) describes the relationships among fundamental traffic variables of flow, density, and speed. FD represents fundamental properties of traffic streams, giving insights into traffic performance. This paper presents a theoretical investigation of dynamic FD properties, derived directly from vehicle car-following (control) models to model traffic hysteresis. Analytical derivation of dynamic FD is enabled by (i) frequency-domain representation of vehicle kinematics (acceleration, speed, and position) to derive vehicle trajectories based on transfer function and (ii) continuum approximation of density and flow, measured along the derived trajectories using Edie's generalized definitions. The formulation is generic: the derivation of dynamic FD is possible with any analytical car-following (control) laws for human-driven vehicles or automated vehicles (AVs). Numerical experiments shed light on the effects of the density-flow measurement region and car-following parameters on the dynamic FD properties for an AV platoon.

Keywords: Automated vehicle, Dynamic fundamental diagram, Traffic hysteresis, Traffic oscillation.

* Corresponding authors. E-mail address: xin.wang@wisc.edu (Xin Wang); sue.ahn@wisc.edu (Soyoung Ahn).

1 Introduction

The traffic fundamental diagram (FD) is a representation of the relationships among fundamental traffic variables of flow, density, and speed. FD describes the fundamental properties of traffic streams, giving insights into traffic performance. Since its inception by the seminal Greenshields model(Greenshields et al., 1935), numerous studies have ensued to confirm its existence(e.g., Ahn et al., 2004; Cassidy, 1998) and determine the shape, giving rise to various families of models(e.g., Newell, 1993; Smulders, 1986; Wu, 2002). FD has been widely used as an important basis for planning and operational analysis (e.g., level of service determination(HCM, 2016), and dynamic traffic management such as ramp metering(e.g., Papageorgiou & Kotsialos, 2002; Papamichail et al., 2010) and variable speed limit (VSL) control(Carlson et al., 2010; Chen et al., 2014a; Chen & Ahn, 2015; Hegyi et al., 2005; Knoop et al., 2010).

The FD, in the traditional sense, describes steady traffic properties and is often referred to as a 'static' traffic model. However, in their seminal empirical study, Treiterer & Myers, (1974) discovered 'traffic hysteresis' - an elliptical evolution of flow-density relationship as vehicles decelerate and accelerate during a major traffic disturbance. Since then, presence of traffic hysteresis has been confirmed and theorized by many studies(Chen et al., 2012; Zhang, 1999), though some studies suggest that the hysteresis magnitude, attributed to car-following, has been exaggerated in earlier studies(e.g., Ahn & Vadlamani, 2010; Coifman et al., 2018; Laval, 2011). Generally, there are two types of hysteresis discussed. The first type stems from traffic oscillations around an equilibrium traffic state in congested traffic. For this type, the initial equilibrium state is restored after the passage of disturbance(Treiterer & Myers, 1974). The other type involves a change in equilibrium state, particularly from uncongested to congested states. A three-phase car following theory by Zhang (1999) and Zhang & Kim (2005) describes this type of traffic hysteresis, where 'capacity drop' phenomenon (i.e., lower throughput after transitioning to a congested state) is emphasized. The present paper focuses on the first type.

In addition, automated vehicles (AVs), with their increasing adoption rate, will likely bring systematic changes to traffic properties, both static and dynamic. Notably, (T. Li et al., 2022) provided a thorough empirical analysis of FD using experimental data from 17 adaptive cruise control (ACC) vehicles using the measurement method developed by Shi & Li (2021). They found that the ACC vehicles exhibit linear FDs (in the congested branch), though the magnitudes of FD parameters can be significantly different from those for human-driven vehicles, depending on the input setting. Further, the experimental study using four different commercial AVs with ACC has verified the existence of traffic hysteresis in AV platoons(Makridis et al., 2021). While insightful, major shortcomings of these experimental studies are that (i) the investigations are limited to static properties, or (ii) the ACC algorithms are proprietary and unknown to the public, thus the underlying mechanisms remain unknown. Notably, some theoretical investigations of FD with AVs exist in the literature(Shi & Li, 2021; Yao et al., 2022; J. Zhou & Zhu, 2020); however, the scope remains largely limited to static properties. Thus, we have a limited understanding of how the control formulation and parameter setting impact dynamic FD features.

Dynamic properties of FD, particularly traffic hysteresis, have important implications for dynamic traffic control. For example, some well-known VSL control methods are based on the first-order kinematic wave (KW) theory(Chen et al., 2014b; Han et al., 2017; Hegyi et al., 2005), in which traffic evolution is described by solving a system of static FD equation and a first-order partial differential equation for flow conservation. These methods determine appropriate speed limits in a dynamic fashion by predicting the traffic states the imposed speed limits will induce. However, the first order KW models assume infinite acceleration/deceleration, thereby failing to capture complex features such as capacity drop, stop-and-go oscillations, and hysteresis observed in real traffic(Logghe & Immers, 2008; Nagel & Nelson, 2005). Higher order KW models introduce an additional partial differential equation to capture finite vehicle acceleration/deceleration (while still working with a static FD)(Aw & Rascle, 2000; Lebacque et al., 2007; H. Payne, 1971; H. J. Payne, 1971; Van Wageningen-Kessels et al., 2015; Zhang, 1999). Owing to this treatment, some of these higher-order KW models can successfully reproduce the above traffic features, including traffic hysteresis. While these models provide a more accurate description of dynamic traffic, their applications for dynamic traffic control have been limited (exception: Carlson et al., 2010) due to their complexity in interpretation, calibration and validation, numerical approximation, and computation.

In this paper, we conduct a theoretical investigation of dynamic FD, a kind that can depict key higher-order, nonlinear traffic features such as traffic hysteresis. It is derived directly from car-following control models for AV to provide direct insight into how vehicle behavior scales up to dynamic traffic behavior, which is currently missing in the literature. We focus on dynamic FD (rather than the KW model), in light of contemporary traffic control strategies, such as reinforcement learning(Han et al., 2022; Li et al., 2017) and control theory(Zhou et al., 2020) based control, that do not necessarily adhere to the KW theory. For these strategies, incorporation of dynamic FD presents a classic and elegant approach to maintain physical validity. We also emphasize the direct connection between vehicle and traffic behavior because connected AVs (CAVs) will likely serve as control actuators in future traffic control. Thus, the linkage provides direct insight into how CAVs should be controlled to achieve a specific traffic performance (e.g., beyond string stability). Further, it can provide a simpler platform for control: desirable vehicle control can be achieved through adjusting control parameter settings, rather than prescribing a precise form of vehicle trajectory. Our framework directly maps the car following law to the dynamic fundamental diagram to provide insight into the mechanisms, which can be harnessed for dynamic traffic management (e.g., ramp metering, and variable speed limit) together with vehicle control.

In this study, analytical derivation of dynamic FD is enabled by (i) frequency-domain representation of vehicle kinematics (acceleration, speed, and position) and (ii) continuum approximation of flow and density measured along the derived trajectory using Edie's generalized definitions(Edie, 1963). The formulation is generic in the sense that derivation of dynamic FD is possible with any analytical car-following (control) laws for human-driven vehicles or AVs. To verify our derivations and identify potential factors affecting dynamic FDs, a series of numerical experiments were conducted. The results show the presence of hysteresis within the AV traffic flow when facing oscillations. The shape and orientation on hysteresis in the dynamic FD are influenced by the frequency characteristics of oscillations (single-frequency or multi-frequency), flow-density measurement region, and the car-following control parameter setting. Particularly, we show that the control gains, total delay in sensing and control actuation, desired time gap, and equilibrium speed all have unique effects on the properties of dynamic FD.

The remainder of this paper is organized as follows. Section 2 presents the trajectory expressions for a CAV platoon in frequency domain. Section 3 then analytically derives fundamental variables in dynamic FD. Simulation experiments and their results to illustrate the efficacy of our dynamic FD are provided in Section 4. Finally, Section 5 contains our conclusions and limitations.

2 Frequency-domain CAV Trajectory

In this section, we mathematically derive the trajectory of CAV based on a transfer function in the frequency domain. The frequency-domain representation can better describe the evolution of oscillations in a platoon, compared to traditional time-domain expressions(Zhou et al., 2023). Further, using a transfer function can unveil the input-output relationship for a time-invariant dynamic system such as the longitudinal control of CAVs.

First, we consider a platoon of N homogenous CAVs, indexed by $l \in \{0,1,\dots,N-1\}$, where 0 indicates the leading vehicle. All CAVs are assumed to follow the same deterministic car-following law, f,

$$a_l(t) = f\big(\Delta x_l(t-\theta), v_l(t-\theta), v_{l-1}(t-\theta)\big), \tag{1}$$

where $a_l(\cdot), v_l(\cdot)$, and $\Delta x_l(\cdot)$ respectively denote vehicle l's acceleration, speed, and spacing with its predecessor over time. In addition, θ denotes the total time delay caused by CAV's sensing and control actuation (i.e., system's latency), we treat it as constant for simplicity. By the physical kinematics law, $\Delta x_l(t) = \int_0^t [v_l(\varphi) - v_{l-1}(\varphi)]d\varphi + \Delta x_l(0)$. To describe car-following under traffic oscillations, we decompose vehicle trajectories into the nominal and the oscillatory components. The former represents an equilibrium state, described by a unique relationship between the equilibrium speed, v_e, and spacing, Δx_e, where v_e varies from 0 to the free flow speed. Both Δx_e and v_e are constants. In this state, $a_l(t) = f(\Delta x_e, v_e, v_e) = 0$. In the following context, we assume the equilibrium state will not change throughout the oscillations. Traffic hysteresis resulting from an equilibrium state change falls beyond the scope of this discussion. The oscillatory component describes the deviation from the equilibrium state, characterized by $\Delta\hat{x}_l(t) := \Delta x_l(t) - \Delta x_e$ and $\hat{v}_l(t) := v_l(t) - v_e$. For convenience, here we linearize the system over the equilibrium point $(\Delta x_e,\ v_e, v_e)$ to analyze the first-order residual impacts of $\big(\Delta\hat{x}_l(t), \hat{v}_l(t), \hat{v}_{l-1}(t)\big)$ on acceleration $a_l(t)$ by letting $\hat{f}\big(\Delta\hat{x}_l(t), \hat{v}_l(t), \hat{v}_{l-1}(t)\big) = f(\Delta x_l(t), v_l(t), v_{l-1}(t))$. $\hat{f}$ is a shifted function of f via shifting $\Delta\hat{x}_l(t), \hat{v}_l(t), \hat{v}_{l-1}(t)$ by Δx_e, v_e, v_e, respectively. Then the equilibrium state is $\hat{f}(0,0,0) = 0$.

We also assume the initial conditions of all following CAVs are at equilibrium, i.e., $\Delta x_l(0) = \Delta x_e, \forall l = 1,2,\dots,N-1$. Without loss of generality, let $x_0(0) = 0$. Then, by the kinematics law, the oscillatory position can be written as:

$$\Delta\hat{x}_l(t) = \int_0^t \hat{v}_l(\varphi)d\varphi - \int_0^t \hat{v}_{l-1}(\varphi)d\varphi. \tag{2}$$

Further, for derivation convenience, we conduct linearization on f. Through a Taylor series expansion near the origin $(0,0,0)$ and ignoring higher order terms as they are very close to zero, f can be linearized as:

$$\hat{f} = a_l(t) = \hat{f}_1{}'\Delta\hat{x}_l(t-\theta) + \hat{f}_2{}'\hat{v}_l(t-\theta) + \hat{f}_3{}'\hat{v}_{l-1}(t-\theta), \tag{3}$$

where $\hat{f}_1'$, $\hat{f}_2{}'$, and $\hat{f}_3{}'$ are gradients, obtained via the first-order partial derivative corresponding to each term; i. e., $\hat{f}_1' = \frac{\partial \hat{f}}{\partial \Delta\hat{x}_l}, \hat{f}_2' = \frac{\partial \hat{f}}{\partial \hat{v}_l}$, and $\hat{f}_3' = \frac{\partial \hat{f}}{\partial \hat{v}_{l-1}}$. Note that $\hat{f}$ is the linear approximation of general nonlinear CF law f.

Combining Eqs. (2) and (3), we have

$$\dot{v}_l(t) = \hat{f}_1{}'\left(\int_0^{t-\theta} \hat{v}_l(\varphi)d\varphi - \int_0^{t-\theta} \hat{v}_{l-1}(\varphi)d\varphi\right) + \hat{f}_2'\hat{v}_l(t-\theta) + \hat{f}_3{}'\hat{v}_{l-1}(t-\theta). \tag{4}$$

For simplification, we further assume $\hat{v}_l(0) = 0$. As Eq. (4) is still highly non-linear, we take the Laplace transform for further derivation of CAV trajectory in the frequency domain. The transformation provides a convenient platform to study a linear dynamic system by substituting integration with division and differentiation with multiplication. Then, Eq. (4) is converted as follows in the frequency domain:

$$s\hat{V}_l(s) - \hat{f}_1{}'\frac{e^{-\theta s}}{s}\hat{V}_l(s) - \hat{f}_2{}'\hat{V}_l(s)e^{-\theta s} = -\hat{f}_1{}'\frac{e^{-\theta s}}{s}\hat{V}_{l-1}(s) + \hat{f}_3{}'\hat{V}_{l-1}(s)e^{-\theta s}, \tag{5}$$

where $s = j\omega$, j denotes the imaginary unit, and ω is the frequency. $\hat{V}_l(s)$ and $\hat{V}_{l-1}(s)$ are respectively the oscillatory speeds of vehicles l and $l-1$ in the frequency domain. Then the xtransfer function, $G(s)$, can be defined using the oscillatory components of speed:

$$G(s) = \frac{\hat{x}_l(s)}{\hat{x}_{l-1}(s)} = \frac{s\hat{V}_l(s)}{s\hat{V}_{l-1}(s)} = \frac{\hat{V}_l(s)}{\hat{V}_{l-1}(s)} = \frac{-\hat{f}_1'e^{-\theta s} + \hat{f}_3'se^{-\theta s}}{s^2 - \hat{f}_1'e^{-\theta s} - \hat{f}_2'se^{-\theta s}}. \tag{6}$$

We write $G(j\omega) = |G(j\omega)|e^{j\measuredangle G(j\omega)}$ with its norm $|G(j\omega)|$ and angle $\measuredangle G(j\omega)$. The transfer function implies how output (i.e. $\hat{V}_l(s)$) responds to the input ((i.e. $\hat{V}_{l-1}(s)$)). It can be used to describe oscillation propagation along a platoon, which is a crucial element to describe dynamic traffic.

Remark 1 The transfer function described above is intricately linked to the norm $|G(j\omega)|$ and the phase shift $\measuredangle G(j\omega)$. The transfer function defined above is intricately linked to the norm $|G(j\omega)|$ and the phase shift $\measuredangle G(j\omega)$ (Zhou et al., 2023). It is noteworthy that the framework established herein remains applicable even in the presence of alternative nonlinear or unidentified car-following laws, where we can replace the transfer function with a describing function(Li et al., 2012, 2014; Li & Ouyang, 2011; Wang et al., 2020) or a data-driven transfer function(Y. Zhou et al., 2023) to approximate the behavior.

Based on the above work, we are ready to derive the position for vehicle l in CAV platoon. Without loss of generality, we assume the position of leading vehicle 0 as follows:

$$x_0(t) = \bar{x}_0(t) + \hat{x}_0(t), \tag{7}$$

Where

$$\bar{x}_0(t) = v_e t, \tag{8}$$

$$\hat{x}_0(t) = \sum_{m=1}^{\infty} A_0^{(m)} \sin(\omega_m t + \phi_m), \tag{9}$$

where $\bar{x}_0(t)$ is the nominal component and $\hat{x}_0(t)$ the oscillation component. Note that we decompose the oscillation into the sum of sinusoidal waves through its Fourier transform; see Eq. (6b). m is the index of oscillatory waves, and $A_0^{(m)}$ is the amplitude of oscillatory wave with frequency ω_m and phase shift ϕ_m. Sinusoidal functions are selected for their advantageous attributes of boundedness and periodicity. We employ the mathematical framework of sinusoidal functions, $\hat{x}_0(t) = \sum_{m=1}^{\infty} A_0^{(m)} \sin(\omega_m t + \phi_m)$, to represent the oscillatory components. We employ multiple sinusoidal waves to model oscillations with compound frequencies to be more realistic. This approach is widely adopted in analytical modeling of waves, as exemplified by Li et al. (2014).

We can also derive the speed and acceleration of the leading vehicle composed of the nominal and oscillatory components:

$$v_0(t) = \bar{v}_0(t) + \hat{v}_0(t) = v_e + A_0^{(m)} \omega_m \sum_{m=1}^{\infty} \cos(\omega_m t + \phi_m), \tag{4}$$

$$a_0(t) = \bar{a}_0(t) + \hat{a}_0(t) = -A_0^{(m)} \omega_m^2 \sum_{m=1}^{\infty} \sin(\omega_m t + \phi_m), \tag{5}$$

By Eq. (6), we can further find $\hat{X}_l(s) = \hat{X}_{l-1}(s)G(s)$. Therefore, given the platoon satisfying the aforementioned initial condition, vehicle l's position has the following nominal and oscillatory components:

$$\bar{x}_l(t) = v_e t - l\Delta x_e, \tag{12}$$

$$\begin{aligned} \hat{x}_l(t) &= \mathcal{L}^{-1}\left(\hat{X}_l(s)\right) = \mathcal{L}^{-1}\left(\hat{X}_0(s)G^l(s)\right) = \mathcal{L}^{-1}\left(\hat{X}_0(s)|G(s)|^l e^{jl\measuredangle G(s)}\right) \\ &= \lim_{M\to\infty} \sum_{m=1}^{M} A_0^{(m)} |G(j\omega_m)|^l \sin\left(\omega_m t + \phi_m + l\measuredangle G(j\omega_m)\right). \end{aligned} \tag{13}$$

Correspondingly, for vehicle l, the speed and acceleration are:

$$v_l(t) = v_e + A_0^{(m)} |G(j\omega_m)|^l \omega_m \sum_{m=1}^{\infty} \cos\left(\omega_m t + \phi_m + l\measuredangle G(j\omega_m)\right) \tag{14}$$

$$a_l(t) = -A_0^{(m)} |G(j\omega_m)|^l \omega_m^2 \sum_{m=1}^{\infty} \sin\left(\omega_m t + \phi_m + l\measuredangle G(j\omega_m)\right) \tag{15}$$

It is noteworthy that the negative sign within the oscillatory component of acceleration (Eq. 15) bears limited consequences, owing to the periodic nature of the sinusoidal function. Then for a platoon consisting of N homogenous CAVs, the length of the platoon can be derived as (after some simplification):

$$x_0(t) - x_N(t) = N\Delta x_e + \sum_{m=1}^{M} R A_0^{(m)} [\sin(\omega_m t + \phi_m - \phi_c)], \tag{6}$$

where $R = \sqrt{1 - 2|G(j\omega_m)|^N \cos\left(N\measuredangle G(j\omega_m)\right) + |G(j\omega_m)|^{2N}}$ and $\phi_c = \arctan \frac{|G(j\omega_m)|^N \sin\left(N\measuredangle G(j\omega_m)\right)}{1 - |G(j\omega_m)|^N \cos\left(N\measuredangle G(j\omega_m)\right)}$ are two constant values. For a comprehensive derivation, please refer to Appendix A.

3 Analytical Model of Dynamic FD

Here we derive the fundamental traffic variables using the position derived in Section 2 and then FD. This approach allows us scale up to dynamic FD while retaining dynamic vehicle characteristics. The discussion of FD pertains to traffic hysteresis within the congested regime. To this end, we first apply Edie's generalized definitions for traffic density and flow (Edie, 1963) since they are flexible for different measurement methods. (In Edie's definition, density is denoted as the total time spent by all N vehicles divided by the area of a measurement time-space region.

Flow is denoted as the total distance travelled by all N vehicles divided by the area of time-space region.) Specifically, the generalized definitions give density and flow as follows:

$$k(t, \Delta t, N) = \frac{N\Delta t}{W(t, \Delta t, N)}, \tag{7}$$

$$Q(t, \Delta t, N) = \frac{\sum_{l=1}^{N}(x_l(t+\Delta t) - x_l(t))}{W(t, \Delta t, N)}, \tag{8}$$

where k and Q are density and flow, respectively. W is the area of a predefined time-space region. Instead of a traditional rectangular window, we define a customized time-space window W at time t along the trajectories covering all N CAVs with a width Δt. This window, depicted in Fig. 1, can be referred to as vertical window[1]. Hence, we have the area as:

$$\begin{aligned} W(t, \Delta t, N) &= \int_{t}^{t+\Delta t}[x_0(t) - x_N(t)]\mathrm{d}t \\ &= N\Delta x_e \Delta t + \sum_{m=1}^{M}\frac{RA_0^{(m)}}{\omega_m}[\cos(\omega_m t + \phi_m - \phi_c) - \cos(\omega_m(t+\Delta t) + \phi_m - \phi_c)]. \end{aligned} \tag{99}$$

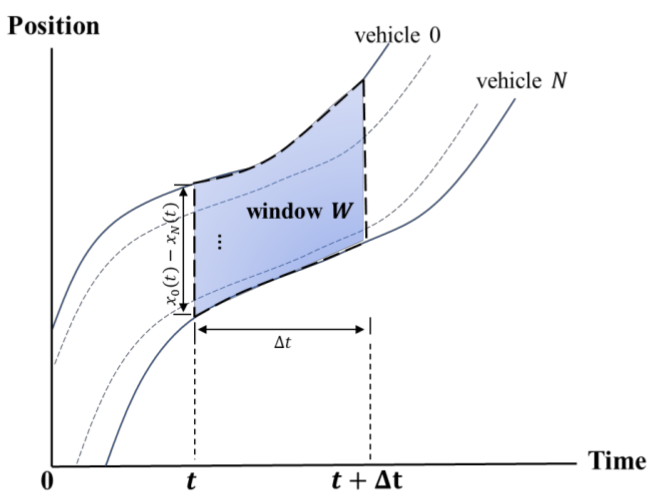

Figure 1: Illustration of vertical time-space window.

This customized window, referred to as the "vertical window," is recognized for its straightforward interpretability and mathematical convenience. Then, combined with Eq. (99), Eqs. (7) and (8) can be rewritten as:

$$k(t, \Delta t, N) = \frac{N\Delta t}{N\Delta x_e\Delta t + \sum_{m=1}^{M}\frac{RA_0^{(m)}}{\omega_m}[\cos(\omega_m t + \phi_m - \phi_c) - \cos(\omega_m(t+\Delta t) + \phi_m - \phi_c)]}, \tag{20}$$

[1] In Laval (2011), the window is slanted according to the maximum congestion wave speed to maximize the chance of having a homogenous traffic state. This paper uses vertical windows instead for mathematical elegance and due to the fact that the wave speed can be nonlinear along the vehicle platoon (considering the disturbance dampening) and potentially time-varying (Shi et al. 2023). This property renders analytical derivation based on slanted windows mathematically prohibitive.

$$Q(t,\Delta t,N)=\frac{Nv_e\Delta t+\sum_{l=1}^{N}\sum_{m=1}^{M}A_0^{(m)}|G(j\omega_m)|^l\left[\sin\left(\omega_m(t+\Delta t)+\phi_m+l\measuredangle G(j\omega_m)\right)-\sin\left(\omega_m t+\phi_m+l\measuredangle G(j\omega_m)\right)\right]}{N\Delta x_e\Delta t+\sum_{m=1}^{M}\frac{RA_0^{(m)}}{\omega_m}\left[\cos\left(\omega_m t+\phi_m-\phi_c\right)-\cos\left(\omega_m(t+\Delta t)+\phi_m-\phi_c\right)\right]}. \tag{21}$$

3.1 Continuum approximation

To make sure that the derived density and flow are physically meaningful and continuous in the time domain, we take the limit, $\boldsymbol{\Delta t\rightarrow 0}$ of Eqs. (20) and (21):

$$k(t,N)=\frac{N}{N\Delta x_e+\sum_{m=1}^{M}RA_0^{(m)}\sin(\omega_m t+\phi_m-\phi_c)}, \tag{22}$$

$$Q(t,N)=\frac{Nv_e+\sum_{l=1}^{N}\sum_{m=1}^{M}A_0^{(m)}|G(j\omega_m)|^l\omega_m\cos(\omega_m t+\phi_m+l\measuredangle G(j\omega_m))}{N\Delta x_e+\sum_{m=1}^{M}RA_0^{(m)}\sin(\omega_m t+\phi_m-\phi_c)}. \tag{23}$$

The result shows that k and Q are cyclic functions, whose periods are the least common multiple of $\frac{2\pi}{\omega_m}$, for $1\leq m\leq M$.

Remark 2 From Eqs. (22) and (23), Q and k are both functions of v_e (typically Δx_e is also a function of v_e), oscillation components $A_0^{(m)}$, ω_m and ϕ_m, as well as AV CF control G. Thus, Q and k together can describe the dynamics of FD directly.

Next, we will further discuss two special scenarios based on the continuum approximation (CA). The first scenario pertains to deriving k and Q for a short oscillating platoon, where an oscillation comprises a single dominant sinusoidal wave. In practice scenarios, even when oscillations involve a combination of waves with varying frequencies, there tends to be one 'dominant wave' where its frequency component has the highest magnitude or power. Identifying the dominant wave can be done through techniques such as Fourier analysis, where an oscillation wave is decomposed into its frequency components using the Fourier transform. The second scenario explores k and Q when the single-wave oscillation evolves along a long string stable platoon. Note that in a string stable platoon system, the system's CF behavior remains controllable even when faced with various disturbances in the environment. String stability is an important and desired property from a safety perspective. Hereafter, we guarantee string stability via constraining the norm of the transfer function.

Scenario I (Short Oscillating Platoon). In the case of a single dominant wave (i.e., $M=1$) with p as the principal frequency component, we have

$$k(t,N)=\frac{N}{N\Delta x_e+RA_0^{(p)}\left|G(j\omega_p)\right|^N\sin(\omega_p t+\phi_p-\phi_c)}, \tag{24}$$

$$Q(t,N)=\frac{Nv_e+\sum_{l=1}^{N}A_0^{(p)}\left|G(j\omega_p)\right|^l\omega_p\cos\left(\omega_p t+\phi_p+l\measuredangle G(j\omega_p)\right)}{N\Delta x_e+RA_0^{(p)}\left|G(j\omega_p)\right|^N\sin(\omega_p t+\phi_p-\phi_c)}. \tag{25}$$

In this case, k and Q are both cyclic functions over t with the same oscillation period of $2\pi/\omega_p$. Within one deceleration-acceleration cycle, we can further compute the expectation of k and Q, respectively. For simplicity, let $\phi_p,\phi_c=0$ as we can adjust the upper bound and lower bound of integral during integration. We further define, $\bar{A} = \frac{RA_0^{(p)}\left|G(j\omega_p)\right|^N}{N}$, where $\bar{A}$ stands for the average magnitude of oscillation through the platoon.

Proposition 1 (density expectation): The expectation of k, $E(k)$, follows $E(k) = \frac{1}{\sqrt{(\Delta x_e)^2-(\bar{A})^2}}$.

Proof:

$$E(k) = \frac{\omega_p}{2\pi}\int_0^{\frac{2\pi}{\omega_p}} k(t,N)\,\mathrm{d}t = \frac{\omega_p}{2\pi}\int_0^{\frac{2\pi}{\omega_p}} \frac{N}{N\Delta x_e + RA_0^{(p)}\left|G(j\omega_p)\right|^N \sin(\omega_p t)}\,\mathrm{d}t =$$

$$\frac{\omega_p}{2\pi}\int_0^{\frac{2\pi}{\omega_p}} \frac{1}{\Delta x_e + \left(RA_0^{(p)}\left|G(j\omega_p)\right|^N/N\right)\sin(\omega_p t)}\,\mathrm{d}t,$$

Letting $\frac{RA_0^{(p)}\left|G(j\omega_p)\right|^N}{N} = \bar{A}$, we have $E(k) = \frac{\omega_p}{2\pi}\int_0^{\frac{2\pi}{\omega_p}} \frac{1}{\Delta x_e + \bar{A}\cdot\sin(\omega_p t)} = \frac{\omega_p}{2\pi}\frac{\frac{2\pi}{\sqrt{(\Delta x_e)^2-(\bar{A})^2}}}{\omega_p} = \frac{1}{\sqrt{(\Delta x_e)^2-(\bar{A})^2}}$. Therefore, we obtain Proposition 1.

$$Q.E.D.$$

Note: when $\left|G(j\omega_p)\right| < 1$ and N is large (e.g., $N = 5$), $\bar{A} \ll \Delta x_e$, therefore, $E(k) \approx \frac{1}{\Delta x_e}$.

Proposition 2 (flow expectation): The expectation of Q, $E(Q) = \frac{v_e}{\sqrt{(\Delta x_e)^2-(\bar{A})^2}}$.

Proof:

$$E(Q) = \frac{\omega_p}{2\pi}\int_0^{\frac{2\pi}{\omega_p}} \frac{Nv_e + \sum_{l=1}^{N} A_0^{(p)}\left|G(j\omega_p)\right|^l \omega_p \cos\left(\omega_p t + l\measuredangle G(j\omega_p)\right)}{N\Delta x_e + RA_0^{(1)}\left|G(j\omega_p)\right|^N \sin(\omega_p t)}\,\mathrm{d}t$$

$$= \frac{\omega_p}{2\pi} v_e \int_0^{\frac{2\pi}{\omega_p}} \frac{1}{\Delta x_e + \bar{A}\sin(\omega_p t)}\,\mathrm{d}t + \frac{\omega_p}{2\pi}\frac{A_0^{(p)}\omega_p}{N}\int_0^{\frac{2\pi}{\omega_p}} \frac{\sum_{l=1}^{N}\left|G(j\omega_p)\right|^l \cos\left(\omega_p t + l\measuredangle G(j\omega_p)\right)}{\Delta x_e + \bar{A}\sin(\omega_p t)}\,\mathrm{d}t$$

$$= \frac{\omega_p}{2\pi} v_e \int_0^{\frac{2\pi}{\omega_p}} \frac{1}{\Delta x_e + \bar{A}\sin(\omega_p t)}\,\mathrm{d}t + \frac{\omega_p}{2\pi}\frac{A_0^{(p)}\omega_p}{N}\sum_{l=1}^{N}\left|G(j\omega_p)\right|^l \int_0^{\frac{2\pi}{\omega_p}} \frac{\cos\left(\omega_p t + l\measuredangle G(j\omega_p)\right)}{\Delta x_e + \bar{A}\sin(\omega_p t)}\,\mathrm{d}t$$

$$= \frac{\omega_p}{2\pi} v_e \frac{2\pi}{\omega_p\sqrt{(\Delta x_e)^2-(\bar{A})^2}} + \frac{\omega_p}{2\pi}\frac{A_0^{(p)}\left|G(j\omega_p)\right|^l \omega_p}{N}\cdot F$$

where $F = \int_0^{\frac{2\pi}{\omega_p}} \frac{\cos\left(\omega_p t + l\measuredangle G(j\omega_p)\right)}{\Delta x_e + \bar{A}\sin(\omega_p t)}\,\mathrm{d}t$. As $\int_0^{\frac{2\pi}{\omega_p}} \frac{\cos\left(\omega_p t + l\measuredangle G(j\omega_p)\right)}{\Delta x_e + \bar{A}\sin(\omega_p t)}\,\mathrm{d}t = 0 (l \in [1, N], l \in Z)$, $F = 0$. Hence, $E(Q) = \frac{v_e}{\sqrt{(\Delta x_e)^2-(\bar{A})^2}}$, we have Proposition 3.

$$Q.E.D.$$

Note: Similarly, when $\left|G(j\omega_p)\right| < 1$ and N is large (e.g., $N = 5$), $\bar{A} \ll \Delta x_e$. Therefore, $E(Q) \approx \frac{v_e}{\Delta x_e}$, which is consistent with the fundamental definition, $E(Q) = v_e E(k)$.

Scenario II (Long String Stable Platoon). Considering a long platoon (i.e., $N \to \infty$) that is string stable (i.e., $\left|G(j\omega_p)\right| < 1$, we have

$$\lim_{N\to\infty} E\big(k(N)\big) = \frac{1}{\Delta x_e},$$

$$\lim_{N\to\infty} E\big(Q(N)\big) = \frac{v_e}{\Delta x_e},$$

which suggests a traditional FD for steady traffic flow. This is intuitive because if the platoon is long enough and string stable, oscillations would be dampened eventually to the equilibrium point.

3.2 Hysteresis orientation

Here we analytically determine the orientation of hysteresis that can arise during an oscillation. Specifically, a random point on the hysteresis loop, referred as p_1, is selected, as depicted in Fig.2. Accordingly, its density and flow at time point t are denoted as $k(t)$ and $Q(t)$. Then, after a small time interval Δt, the corresponding point on the loop is denoted as p_2, characterized by density $k(t+\Delta t)$ and flow $Q(t+\Delta t)$. The equilibrium point is expressed as $Eq(k_e, Q_e)$, where k_e and Q_e are respectively the equilibrium density and flow. Then, we can define two vectors $\vec{\boldsymbol{a}}$ and $\vec{\boldsymbol{b}}$ to describe the directional segments towards p_1 and p_2, respectively, from the equilibrium point: $\vec{\boldsymbol{a}}$: $(k(t)-k_e, Q(t)-Q_e)$, $\vec{\boldsymbol{b}}$: $(k(t+\Delta t)-k_e, Q(t+\Delta t)-Q_e)$.

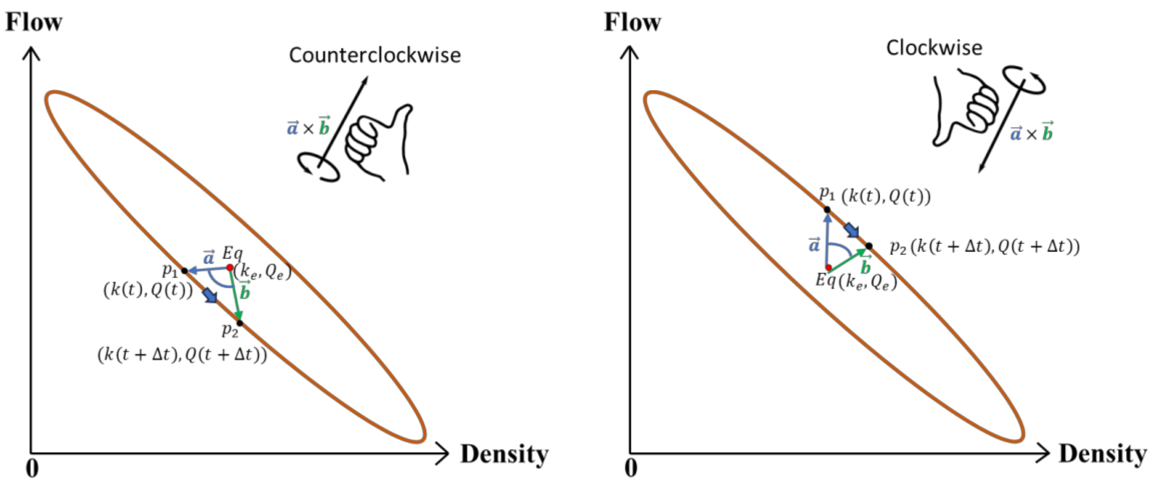

(a) (b)

Figure 2: Example of traffic hysteresis orientation (a) counter-clockwise and (b) clockwise

Then to find the hysteresis direction, we take the cross product of $\vec{\boldsymbol{a}}$ and $\vec{\boldsymbol{b}}$ and then apply the right-hand rule. $\vec{\boldsymbol{a}}\times\vec{\boldsymbol{b}}$ can be expressed as determinant:

$$\vec{\boldsymbol{a}}\times\vec{\boldsymbol{b}} = \begin{vmatrix} k(t)-k_e & Q(t)-Q_e \\ k(t+\Delta t)-k_e & Q(t+\Delta t)-Q_e \end{vmatrix}. \tag{26}$$

Eq. (20) can be further written as $\vec{\boldsymbol{a}}\times\vec{\boldsymbol{b}} = (Q(t+\Delta t)-Q_e)(k(t)-k_e) - (Q(t)-Q_e)(k(t+\Delta t)-k_e)$. After reorganizing, we obtain,

$$\vec{\boldsymbol{a}}\times\vec{\boldsymbol{b}} = Q(t+\Delta t)(k(t)-k_e) - k(t+\Delta t\,)(Q(t)-Q_e) + Q(t)k_e - k(t)Q_e. \tag{27}$$

From **Scenario II**, $k_e = \frac{1}{\Delta x_e}$ and $Q_e = \frac{v_e}{\Delta x_e}$. And by combining Eq. (26) and Eq. (27) from **Scenario I**, we obtain (after some simplification)

$$\vec{\boldsymbol{a}} \times \vec{\boldsymbol{b}} = \frac{A_0^{(p)}\omega_p}{N\Delta x_e}\left[\frac{\sum_{\boldsymbol{l=1}}^{\boldsymbol{N}}\left|G(j\omega_p)\right|^l \cos\left(\omega_p t+\phi_p+l\measuredangle G(j\omega_p)\right)}{\Delta x_e+\bar{A}\sin(\omega_p t+\phi_p-\phi_c)} - \frac{\sum_{\boldsymbol{l=1}}^{\boldsymbol{N}}\left|G(j\omega_p)\right|^l \cos\left(\omega_p (t+\Delta t)+\phi_p+l\measuredangle G(j\omega_p)\right)}{\Delta x_e+\bar{A}\sin(\omega_p (t+\Delta t)+\phi_p-\phi_c)}\right]. \tag{28}$$

Proposition 3 (hysteresis orientation identification). The hysteresis loop evolves clockwise on a dynamic FD if $\sum_{\boldsymbol{l=1}}^{\boldsymbol{N}}\left|G(j\omega_p)\right|^l \cos\left(l\measuredangle G(j\omega_p)+\phi_c\right) < 0$ and counter-clockwise if $\sum_{\boldsymbol{l=1}}^{\boldsymbol{N}}\left|G(j\omega_p)\right|^l \cos\left(l\measuredangle G(j\omega_p)+\phi_c\right) > 0$. Obviously, there is no hysteresis if $\sum_{\boldsymbol{l=1}}^{\boldsymbol{N}}\left|G(j\omega_p)\right|^l \cos\left(l\measuredangle G(j\omega_p)+\phi_c\right) = 0$.

Proof:

Consider $f(t) = \frac{\sum_{\boldsymbol{l=1}}^{\boldsymbol{N}}\left|G(j\omega_p)\right|^l \cos\left(\omega_p t+\phi_p+l\measuredangle G(j\omega_p)\right)}{\Delta x_e+\bar{A}\sin(\omega_p t+\phi_p-\phi_c)}$, then $\vec{\boldsymbol{a}} \times \vec{\boldsymbol{b}} = \frac{A_0^{(p)}\omega_p}{N\Delta x_e}[f(t) - f(t+\Delta t)]$. To investigate the orientation, it is necessary to examine the positivity of $\vec{\boldsymbol{a}} \times \vec{\boldsymbol{b}}$. Consider in one cycle, $i.e., t \in \left[0, \frac{2\pi}{\omega_m}\right]$, since $\frac{A_0^{(p)}\omega_p}{N\Delta x_e}$ is always positive definite, and $f(t+\Delta t) = f(t) + f'(t) * \Delta t$ when $\Delta t \to 0$ (first order approximation), we can rewrite $\vec{\boldsymbol{a}} \times \vec{\boldsymbol{b}} = \frac{A_0^{(p)}\omega_p}{N\Delta x_e}[-f'(t) * \Delta t]$, where $f'(t)$ represents the first order derivative of $f(t)$. Thus, $\vec{\boldsymbol{a}} \times \vec{\boldsymbol{b}} > 0$ when $f'(t) < 0$, otherwise, $\vec{\boldsymbol{a}} \times \vec{\boldsymbol{b}} < 0$ when $f'(t) > 0$. According to the quotient rule,

$$f'(t) = \frac{-\sum_{\boldsymbol{l=1}}^{\boldsymbol{N}}\left|G(j\omega_p)\right|^l \omega_p \sin\left(\omega_p t+\phi_p+l\measuredangle G(j\omega_p)\right) * \left(\Delta x_e+\bar{A}\sin(\omega_p t+\phi_p-\phi_c)\right) - \sum_{\boldsymbol{l=1}}^{\boldsymbol{N}}\left|G(j\omega_p)\right|^l \cos\left(\omega_p t+\phi_p+l\measuredangle G(j\omega_p)\right) * (\bar{A}\omega_p)\cos(\omega_p t+\phi_p-\phi_c)}{\left(\Delta x_e+\bar{A}\sin(\omega_p t+\phi_p-\phi_c)\right)^2}. \tag{29}$$

In Eq. (23), since the denominator of $f'(t) > 0$ always holds, we will only focus on the numerator. Let $\alpha = \omega_p t + \phi_p + l\measuredangle G(j\omega_p)$ and $\beta = \omega_p t + \phi_p - \phi_c$. Then the numerator of Eq. (23) can be written as:

$$\begin{aligned} & -\sum_{l=1}^{N}\left|G(j\omega_p)\right|^l \omega_p \sin\alpha * (\Delta x_e + \bar{A}\sin\beta) - \sum_{l=1}^{N}\left|G(j\omega_p)\right|^l \cos\alpha * (\bar{A}\omega_p)\cos\beta \\ & = -\omega_p \Delta x_e \sum_{\boldsymbol{l=1}}^{\boldsymbol{N}}\left|G(j\omega_p)\right|^l \sin\left(\omega_p t + \phi_p + l\measuredangle G(j\omega_p)\right) - \omega_p \bar{A}\sum_{\boldsymbol{l=1}}^{\boldsymbol{N}}\left|G(j\omega_p)\right|^l \cos\left(l\measuredangle G(j\omega_p) + \phi_c\right) \end{aligned} \tag{30}$$

Regarding the first term in Eq. (23), it should be noted that for each vehicle l within one cycle, $E\left(\left|G(j\omega_p)\right|^l \sin\left(\omega_p t + \phi_p + l\measuredangle G(j\omega_p)\right)\right) = 0$. This result arises from the cyclic property of a sinusoidal function. Therefore $E\left(\sum_{\boldsymbol{l=1}}^{\boldsymbol{N}}\left|G(j\omega_p)\right|^l \sin\left(\omega_p t + \phi_p + l\measuredangle G(j\omega_p)\right)\right) = \boldsymbol{0}$. As a result, the sign of Eq. (24) will only be determined by the second term $-\omega_p \bar{A}\sum_{\boldsymbol{l=1}}^{\boldsymbol{N}}\left|G(j\omega_p)\right|^l \cos\left(l\measuredangle G(j\omega_p) + \phi_c\right)$. According to the right-hand rule, $\vec{\boldsymbol{a}} \times \vec{\boldsymbol{b}} > 0$ corresponds to CCW (Fig. 2(a)), while $\vec{\boldsymbol{a}} \times \vec{\boldsymbol{b}} < 0$ corresponds to CW (Fig. 2(b)).

$$Q.E.D.$$

Note that as $A_0^{(p)}, \omega_p$, and N are all positive, and the orientation of hysteresis loop is only determined by $\left|G(j\omega_p)\right|$ and $\measuredangle G(j\omega_p)$.

4 Numerical Experiments

This section presents a series of numerical experiments to demonstrate how the derived analytical model of dynamic FD works. We start with the experiment setup and demonstrate how CA for FD can effectively represent traffic hysteresis. We further examine the individual and joint effects of key model parameters on the properties of dynamic FD. Through these experiments, we gain a deeper understanding of how the CAV behavior during an oscillation manifests itself in the hysteresis pattern. In addition, to show the generality of our framework, we put the derivation process of an HDV model and provide a comparison with AVs in Appendix B.

4.1 Numerical experiment setup

For the experiments, we adopt the second-order linear feedback controller by Van Arem et al. (2006) for the AV car-following law, as an example. This controller marks the pioneering car-following logic specifically designed for CAV. It is simple yet effective, finding wide adoption in the literature.

The control system state at time t is defined as $[\Delta x_e(t) - \Delta x_l(t),\ v_{l-1}(t) - v_l(t)]^T$, where the first term is the deviation from equilibrium (desired) spacing and the second term is speed difference, T denotes transpose. Here, we incorporate two gains: spacing feedback gain k_s and speed deviation gain k_v. These gains are time-invariant and utilized to regulate the deviation from equilibrium spacing and the speed difference, respectively. Thus, the acceleration is given by:

$$a_l(t) = k_s \cdot \big(\Delta x_e(t) - \Delta x_l(t)\big) - k_v \cdot v_l(t) + k_v \cdot v_{l-1}(t). \tag{31}$$

Note that the acceleration gain is not considered here as AV lacks access to feedforward information from the preceding vehicle. Nevertheless, the proposed analytical model is general and can be extended to the application of CAV. The equilibrium spacing uses the widely adopted constant time gap policy: $\Delta x_e\,(t) = v_e(t) \times \tau + s_0$, where τ and s_0 represent constant desired time gap and standstill spacing, respectively.

Based on Eq. (3) and Eq. (31), we can further derive $\hat{f}_1' = \frac{\partial a_l(t)}{\partial \Delta \hat{x}_l(t)} = \frac{\partial k_s \cdot (-\Delta \hat{x}_l(t))}{\partial \Delta \hat{x}_l(t)} = -k_s$, $\hat{f}_2' = \frac{\partial a_l(t)}{\partial \hat{v}_l(t)} = \frac{\partial(-k_s(v_l(t)\times\tau+s_0)-k_v\cdot v_l(t))}{\partial \hat{v}_l(t)} = -k_v - k_s\tau$, $\hat{f}_3' = \frac{\partial a_l(t)}{\partial \hat{v}_{l-1}(t)} = \frac{\partial(k_v\cdot v_{l-1}(t))}{\partial \hat{v}_{l-1}(t)} = k_v$. Note that the partial derivatives are only related to the oscillatory parts $(\Delta\hat{x}_l(t), \hat{v}_l(t), \hat{v}_{l-1}(t))$ instead of the nominal parts $(\Delta\bar{x}_l(t), \bar{v}_l(t), \bar{v}_{l-1}(t)$.

Then, the corresponding transfer function is given as:

$$G(j\omega) = \frac{\hat{V}_l(j\omega)}{\hat{V}_{l-1}(j\omega)} = \frac{k_s e^{-j\theta\omega} + jk_v\omega e^{-j\theta\omega}}{-\omega^2 + k_s e^{-j\theta\omega} + j(k_v + k_s\tau)\omega e^{-\theta j\omega}}. \tag{32}$$

As an example, we set $k_s = 1\ (s^{-2})$, $k_v = 1(s^{-1})$, $\tau = 0.8\ s$, $v_e = 10m/s$, $\theta = 0.5sec$. See Table 1 for details. Section 4.3 provides an in-depth exploration of the implications of parameter settings on dynamic FDs, where the parameters are set based on previous empirical studies(Gunter et al., 2020, 2021). The total study period is 40 sec and the platoon size, N, is 20. Note that this setting serves as the default configuration for all subsequent experiments unless otherwise specified (i.e., Single oscillation case in Table 1).

Table 1: Default settings

Parameters		Values	
Spacing deviation gain k_s		$1(s^{-2})$	
Speed difference gain k_v		$1(s^{-1})$	
Desired time gap τ		$0.8(s)$	
Equilibrium speed v_e		$10(m/s)$	
Equilibrium spacing x_e		$13(m)$	
Standstill spacing s_0		$5(m)$	
Vehicle number in the platoon N		20	
Total study period T		$40(s)$	
Single oscillation case		**Compound oscillation case**	
Total time delay θ_1	$0.5(s)$	θ_1, θ_2	$0.5(s), 0.3(s)$
Frequency ω_1	$0.1\pi(Hz)$	ω_1, ω_2	$0.1\pi(Hz),$
Phase shift ϕ_1	$\pi/2(°)$	ϕ_1, ϕ_2	$\pi/2(°), 0(°)$
Amplitude $A_0^{(1)}$	$10m$	$A_0^{(1)}, A_0^{(2)}$	$10m, 3m$

4.2 Effects of measurement region

Here we investigate the effects of various parameters on the features of dynamic FD. We first examine the effects of the measurement region, in terms of the width of time window and the platoon size, on the traffic hysteresis under single-frequency and compound (i.e., multi-frequency) oscillations.

Width of time window

We first analyze a case with a single-frequency oscillation. As an example, we set $\omega_1 = 0.1\pi\ Hz$, $\phi_1 = \frac{\pi}{2}$, and oscillation magnitude $A_0^{(1)} = 10m$. Then, we have $|G(j\omega_p)| = 0.9917$ and $\measuredangle G(j\omega_p) = -0.2429\ sec$. To examine the effectiveness of CA, we vary the width of time window, $\Delta t = \{5, 2, 1, 0.1, 0\}\ sec$, where $\Delta t = 0\ sec$ representing CA. The results are shown in Fig. 3. Notably, all FDs evolve clockwise over time, displaying evident hysteresis around the equilibrium point. Further, we observe a noticeable transformation in the shape of the hysteresis as Δt decreases, transitioning from a polygon to an ellipse. This indicates that reducing the window width allows for a more precise measurement of the hysteresis and that the proposed CA method for measurement is highly desired. A large Δt (e.g., $\Delta t = 5s$) evidently underestimates the hysteresis.

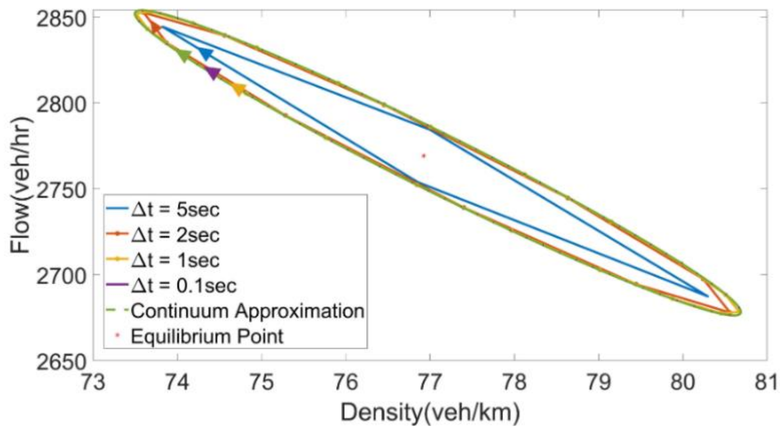

Figure 3: Dynamic FD of different Δt and continuum approximation: Single-frequency oscillation

We further extend our investigation to compound oscillations. This is accomplished by adding another oscillation component with $\omega_2 = 0.3\pi\ Hz$, $A_0^{(2)} = 3m$, and $\phi_2 = 0$. Moreover, we set $\theta = 0.3sec$. The window width is also varied at $\Delta t = \{5, 2, 1, 0.1, 0\}\ sec$. The results are given in Fig. 4. Compared with the single-frequency oscillation case, the shapes of hysteresis loops with compound oscillations are less regular, albeit still cyclic. Furthermore, under the compound oscillations, the underestimation of hysteresis is more pronounced with greater Δt (e.g., 60.45% underestimation of the loop area for $\Delta t = 5sec$, as opposed to 48.47% in the single-frequency case). The CA-based measurement remains effective in capturing the comprehensive hysteresis phenomenon. As per the finding, subsequent experiments are conducted based on the CA method.

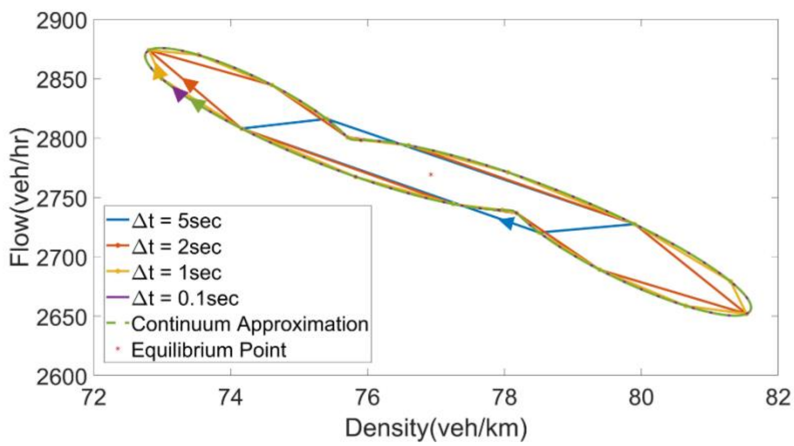

Figure 4: Dynamic FD of different Δt and continuum approximation: Compound oscillations

Platoon size

Here we investigate the effect of the platoon size (N) on the dynamic FD (based on CA). Fig. 5(a) and 5(b) illustrate the effect for string stable and string unstable platoons, respectively. For the former, we use the default setting. For the string unstable platoons, however, we modify both k_s and k_v to 0.5, which gives $\left|G\left(j\omega_p\right)\right| = 1.0847 > 1$ and $\measuredangle G\left(j\omega_p\right) = -0.2818$sec. In Fig. 5(a) and 5(b), we see that each FD evolves clockwise as an ellipse over time. The regularity in shape (perfect ellipse) is attributed to the single-frequency oscillation and the assumption of time-invariant and deterministic CF behavior. It is worth noting that the loop areas for the string unstable platoons are generally much larger than the string stable ones. Further, from Fig. 5(a), the movement area, in terms of both ellipsoidal length and width, decreases as N increases because $|G(j\omega_p)| < 1$, causing the oscillation to be dampened over space. Conversely, in Fig. 5(b), the hysteresis loop area expands as N increases, suggesting the oscillation being amplified through the platoon.

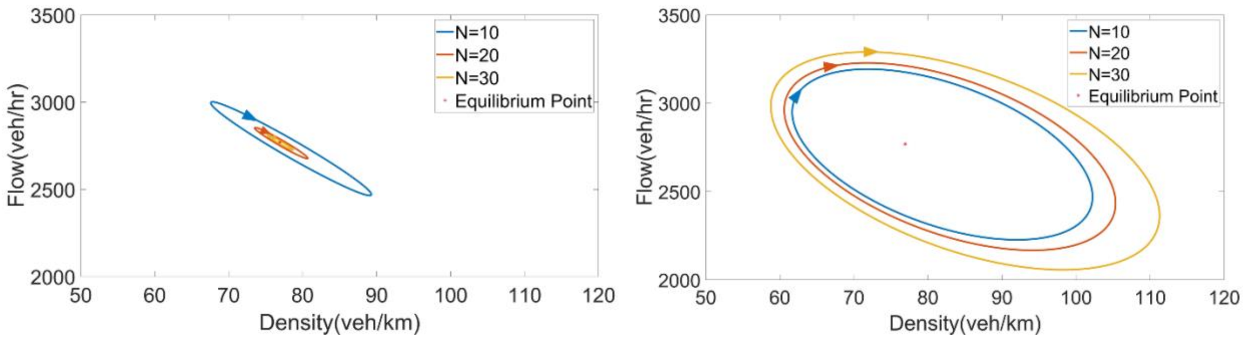

(a) (b)

Figure 5: CA Dynamic FD with different N: (a) string stable $\left(|G(j\omega_p)| = 0.9917\right)$ and (b) string unstable $\left(|G(j\omega_p)| = 1.0847\right)$

4.3 Effects of car-following (control) parameters

This subsection aims to unveil the impact of the car-following control parameter setting on the dynamic FD. Specifically, the control gains, total time delay in sensing and control actuation, desired time gap, and equilibrium speed are explored.

Control gains

To analyze the impact of the control gain setting on the dynamic FD, we conduct a twofold investigation: (i) the effect of each control gain and (ii) the joint effect of two control gains. we vary the values of k_s and k_v based on the feasible regions identified in Kontar et al. (2021). Specifically, we vary them from 1 to 2 with an increment of 0.5. (The units for k_s and k_v are respectively $\sec^{-2}$ and $\sec^{-1}$.)The result for k_s is shown in Fig. 6(a). Notably, an increase in spacing feedback gain leads to a reduction of the hysteresis loop. This can be attributed to the fact that a larger k_s results in a stronger response to a deviation from the equilibrium spacing, leading to less fluctuations and a smaller hysteresis loop.

The impact of k_v is shown in Fig. 6(b). Interestingly, unlike k_s, k_v mainly affects the slope (congested wave speed), with a higher value of k_v indicating a higher wave speed. Since k_v is responsible for regulating the speed difference, a higher sensitivity to the speed difference (i.e., a higher k_v) leads to a quicker response, leading to a higher observed wave speed. This is consistent with the finding in Kontar et al. (2021).

To quantify the features of hysteresis loops in Fig. 6, other than the ranges of density and flow (i.e., $k_{range} = k_{max} - k_{min}, Q_{range} = Q_{max} - Q_{min}$), we further define the width, length, and the area of each loop as illustrated in Fig. 7. Besides, the average wave speed in the congested branch (i.e., $w = \frac{Q_{min} - Q_{max}}{k_{max} - k_{min}}$) is also reported. The results presented in Table 2 show that changing k_s affects both width and length of the ellipsoidal loop, while changing k_v mainly affects the length of hysteresis. Note that the area initially decreases and then increases as k_v increases. This phenomenon is primarily attributed to a change in the orientation of hysteresis loop from clockwise to counter-clockwise. Theoretically, the area would become zero (reducing to a traditional linear relationship) where this change in orientation occurs. We will put more emphasis on the orientation later in the joint influence.

The above findings underscore the difference between the traditional zero-order (static) FD and our dynamic FD, which possesses the capability to capture higher-order traffic flow features.

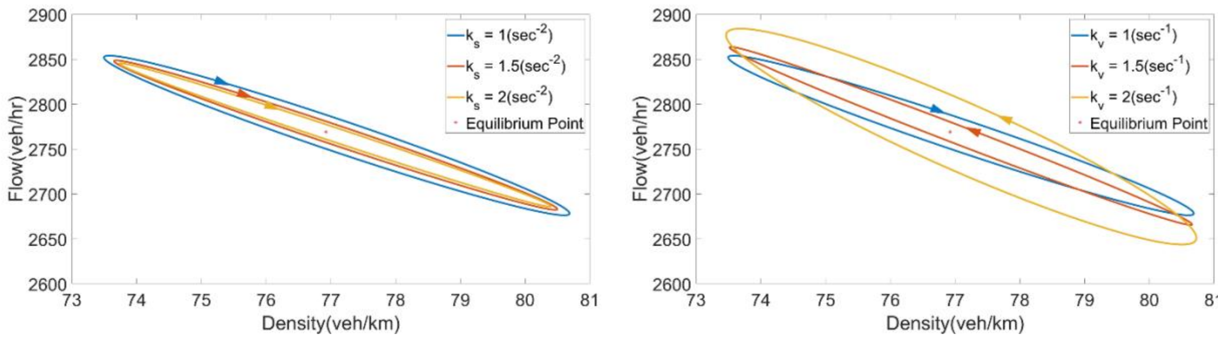

(a) (b)

Figure 6: Dynamic FD with different control parameters (a) k_s and (b) k_v $(\tau = 0.8s, v_e = 10m/s, \theta = 5sec, k_s = 1s^{-1})$

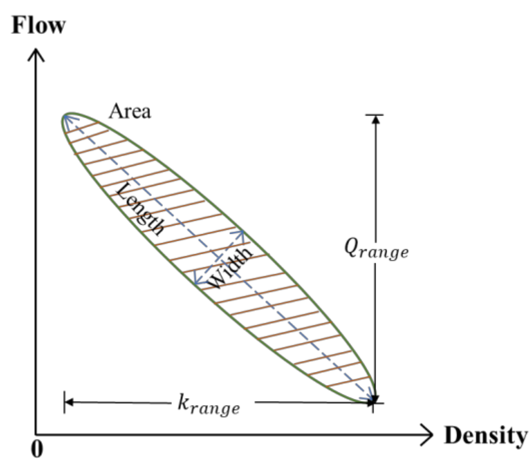

Figure 7: Illustration of hysteresis loop length, width, area, and range

Table 2: Traffic hysteresis measures with respect to (k_s, k_v)

	$k_s(\text{sec}^{-2})$			$k_v(\text{sec}^{-1})$		
	1	1.5	2	1	1.5	2
	$k_e = 76.92(veh/km),\ Q_e = 2769.23(veh/hr)$					
$k_{range}(veh/km)$	7.12	6.84	6.67	7.12	6.96	7.10
$Q_{range}(veh/hr)$	170.79	163.44	158.75	170.79	190.05	238.00
$Maximum\ flow$ $(Q_{max}, veh/hr)$	2854.03	2848.79	2845.69	2854.03	2863.84	2884.13
$Width(veh/km)$	14.28	13.64	13.30	14.28	14.25	14.29
$Length(veh/hr)$	177.27	166.02	159.36	177.27	197.96	240.11
$Area(veh^2/(km \cdot hr))$	213.91	125.77	82.61	213.91	117.33	473.86
$\overline{w}(km/hr)$	−23.97	−23.91	−23.83	−23.97	−27.32	−33.51

We are further interested in the joint influence of control gains over the dynamic FD as they are designed to work together. To explore this systematically, we expand the range of both k_s and k_v to [0.5, 3.0] with a step size of 0.1. Fig. 8 provides a heatmap of the hysteresis orientation with respect to k_s and k_v. From the figure, two distinct boundaries are notable where the orientation switches from clockwise (noted as CW in the figure) to counter-clockwise (CCW) and vice versa. A significant majority (approximately 70%) of these loops exhibit a counter-clockwise pattern. This finding diverges from the conclusion drawn in the empirical study by Ahn et al. (2013) for human-driven vehicles, where clockwise loops are predominantly observed.

Fig. 9 presents the results of a sensitivity analysis, illustrating the performances of the CAV system for different (k_s, k_v) pairs within a physically reasonable range of [1.0, 3.0]. Notably, we have adjusted the lower bound for k_s and k_v to 1.0, as small values of k_s and k_v indicate an unresponsive controller, which is undesired. From Fig. 9(a), we observe that $|G|$ demonstrates a monotonically decreasing trend as k_v increases. Conversely, for k_s, $|G|$ initially experiences a decline until reaching a minimum value at $k_s = 1.1$, subsequently ascending as k_s further increases. In Fig. 9(b), the z-axis is reversed to provide a visual representation of the response time (i.e., the absolute value of $\measuredangle G$). Notably, the system exhibits the shortest response time when k_s is relatively small and k_v is large. This observation suggests that the system's damping characteristics are more pronounced when employing lower values of k_s in conjunction with higher values of k_v. Besides, the range of density in hysteresis is more affected by the setting of k_s than k_v (Fig. 9(c)). The behavior of density is non-monotonic, with the combination of $k_s = 3$ and $k_v = 1.4$ yielding the minimum density range. The same trend holds for the flow range, where the optimal combination is $k_s = 3$ and $k_v = 1.1$ (Fig. 9(d)).

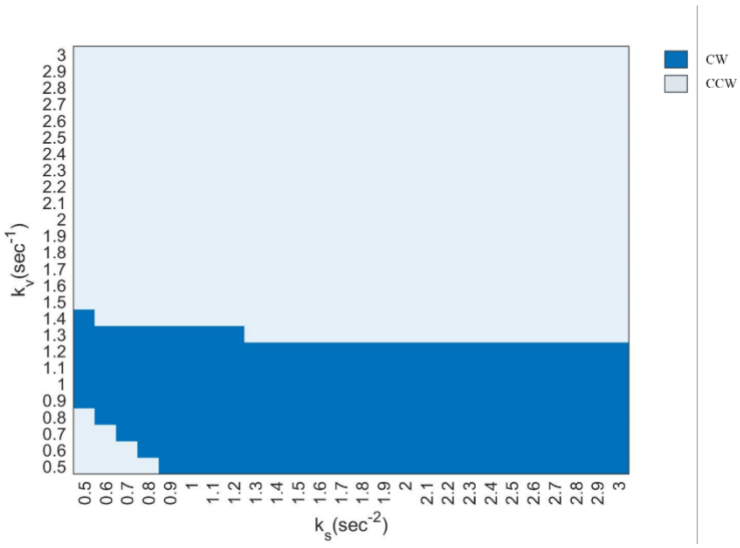

Figure 8: Heatmap for hysteresis orientation with varying (k_s, k_v) $(\tau = 0.8s, v_e = 10m/s, \theta = 5sec)$

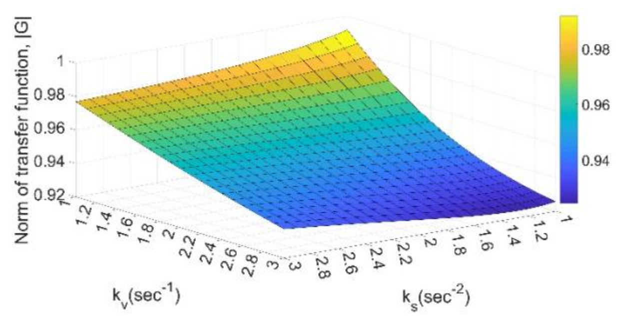

(a)

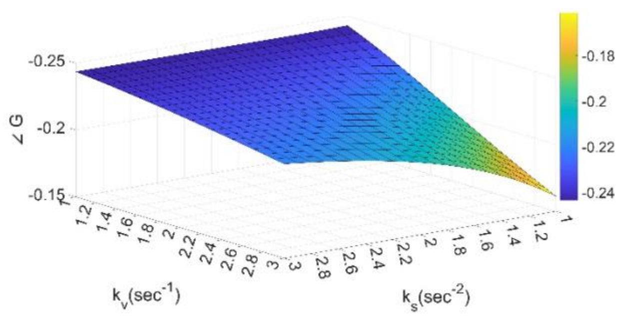

(b)

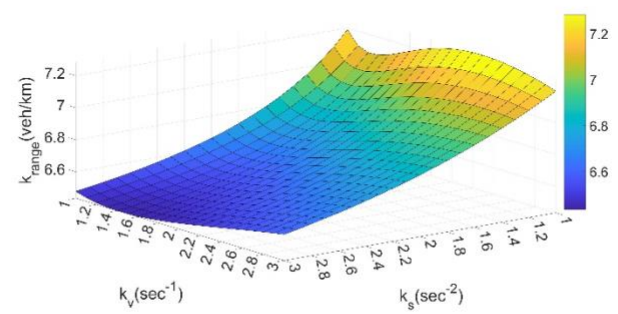

(c)

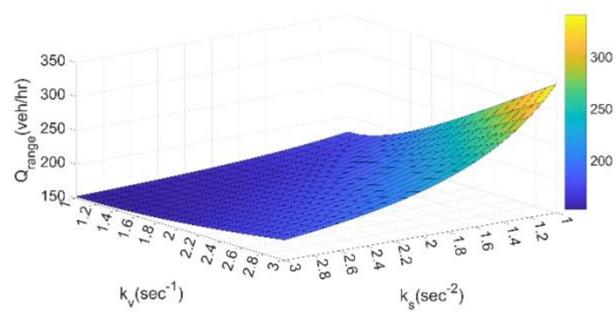

(d)

Figure 9: Performances with varying (k_s, k_v) in terms of (a) norm of transfer function, (b) angle of transfer function, (c) range of density, and (d) range of flow

Other parameters

Next, the individual impacts of the total time delay (θ), desired time gap (τ), and equilibrium speed (v_e) on the dynamic FD are investigated. Fig. 10(a) illustrates the effect of the time delay ($0.5sec$, $1sec$, $1.5sec$), revealing that an increase in delay leads to a deterioration in the platoon's performance, accompanied by a larger hysteresis loop and higher wave speed. This is intuitive since a larger delay in sensing and control actuation is known to make the system unstable (M. Wang, 2018).

For the desired time gap (set to $0.8sec$, $0.9sec$, and $1sec$), the result in Fig. 10(b) shows that a tighter time gap (e.g., $\tau = 0.8sec$) yields higher flow and density, albeit at the expense of a larger hysteresis loop. This observation is also intuitive since maintaining a tighter spacing gives a smaller room for error, leading to system instability. This also suggests that a dynamic FD is particularly useful under more aggressive settings, in which traffic hysteresis can arise.

Table 3 exhibits the quantitative measures of performance obtained through varying θ and τ. Notice that increasing θ also increases the wave speed. And when τ is set to $1sec$, the hysteresis loop area is very small and approaches a linear pattern. This indicates that employing a more conservative (larger) desired time gap setting will lead to a more static traditional linear FD relationship.

Fig. 10(c) shows the dynamic FD with the equilibrium speed varying from $5m/s$ to $13m/s$ with an increase of $2\ m/s$. Notably, the slope from the origin to the equilibrium point of each hysteresis loop represents the value of v_e. Since v_e does not affect the hysteresis orientation (see Eq. (21)), all FDs in Fig. 10(c) are clockwise. Table 4 further provides quantitative measures of performances of different v_e. It is noteworthy that the setting of v_e can have a significant impact on dynamic FD, as reflected by the area change. Further, the average wave speed tends to increase with v_e, albeit at a smaller magnitude.

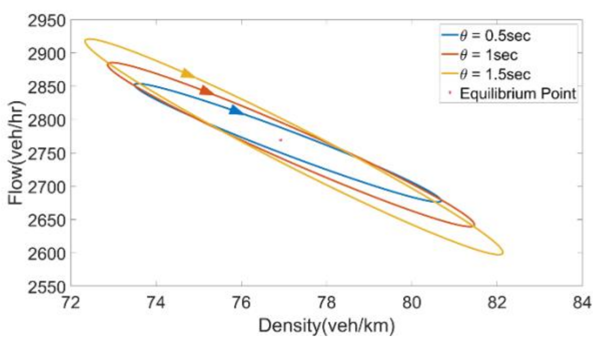

(a)

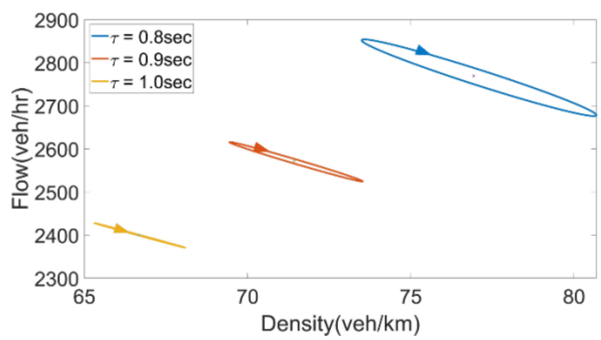

(b)

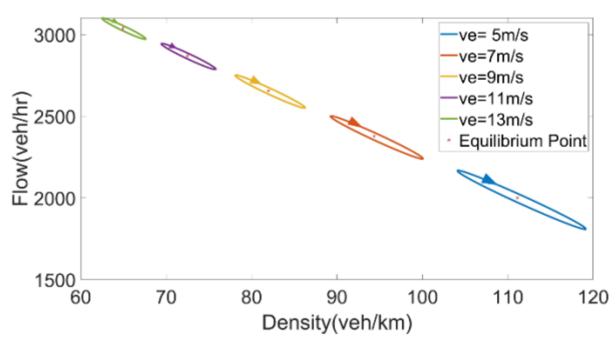

(c)

Figure 10: Dynamic FD with different (a) time delay $(\theta)(\tau = 0.8s, v_e = 10m/s)$, (b) desired time gap $(\tau)(v_e = 10m/s, \theta = 5sec)$, and (c) equilibrium speed (v_e) $(\tau = 0.8s, \theta = 5sec)$

Table 3: Traffic hysteresis measures with respect to θ and τ

	$\theta(\text{sec})$			$\tau(\text{sec})$		
	0.5	1	1.5	0.8	0.9	1
$k_e(veh/km)$	76.92	76.92	76.92	79.62	71.43	66.67
$Q_e(veh/hr)$	2769.23	2769.23	2769.23	2769.23	2571.43	2400.00
$k_{range}(veh/km)$	7.12	8.60	9.78	7.12	4.07	2.64
$Q_{range}(veh/hr)$	170.79	236.88	320.49	170.79	90.31	54.78
$Maximum\ flow$ $(Q_{max}, veh/hr)$	2854.03	2885.64	2920.93	2854.03	2615.85	2427.96
$Width(veh/km)$	14.28	17.10	19.48	14.28	8.13	5.54
$Length(veh/hr)$	177.27	245.76	323.06	177.27	91.16	56.90
$Area(veh^2/(km \cdot hr))$	213.91	337.49	457.70	213.91	34.46	3.66
$\overline{w}(km/hr)$	−23.97	−27.57	−32.79	−23.97	−22.17	−20.77

Table 4: Traffic hysteresis measures with respect to v_e

	$v_e(m/s)$				
	5	7	9	11	13
$k_e(veh/km)$	111.11	94.34	81.97	72.46	64.94
$Q_e(veh/hr)$	2000.00	2377.36	2655.74	2869.57	3038.96
$k_{range}(veh/km)$	15.04	10.83	8.17	6.38	5.12
$Q_{range}(veh/hr)$	359.66	262.28	200.47	158.75	129.22
$Maximum\ flow$ $(Q_{max}, veh/hr)$	2167.85	2501.11	2751.10	2945.54	3101.10
$Width(veh/km)$	29.96	21.55	16.24	12.67	10.15
$Length(veh/hr)$	358.73	261.62	199.98	158.37	128.92
$Area(veh^2/(km \cdot hr))$	581.91	500.56	391.37	295.13	243.26
$\overline{w}(km/hr)$	−23.91	−24.22	−24.54	−24.88	−25.24

5 Conclusions

FDs have been extensively analyzed for decades, mainly for human-driven vehicles. Recently, the advent of AVs has challenged the applicability of classic static FDs as they do not fully capture the higher-order characteristics, such as traffic hysteresis, of AV car-following control. To fill this gap, this paper analytically formulated dynamic FD, based on an analytical car-following control law. The frequency domain representation of the car-following law as a transfer function simplified mathematical derivations. We further applied CA for the derived dynamic FD to provide more accurate, higher-resolution evolution of flow-density relationship over time and incorporate higher-order features. The derived dynamic FD enabled a systematic investigation into the presence of traffic hysteresis in AV platoons and potential factors that impact AV FDs. To systematically determine the orientation of traffic hysteresis, a right-hand rule based criterion was presented.

We conducted a series of numerical experiments to verify the analytical results and examine the properties of the derived dynamic FD with respect to various parameters. First, we investigated the effects of the flow-density measurement region, expressed by the width of time window and the platoon size. The results suggest that a large time window can lead to underestimation of hysteresis, underscoring the importance of using CA. The underestimation was more pronounced with compound oscillations, consisting of multiple frequency components. We also provided some quantitative insights into the impact of car-following control parameter setting on the properties of dynamic FD. Specifically, the control gains, particularly the gain that regulates speed difference, significantly impact the hysteresis magnitude, orientation, and the average wave speed. Further, the delay in sensing and control actuation, desired time gap, and equilibrium speed were all found to have unique impacts on the hysteresis properties. Understanding these effects would be crucial for optimizing the platoon behavior in various traffic scenarios and effectively managing traffic flow.

Some future studies are nonetheless desirable. First, in this study, we focus on the congested regime of pure AV traffic for analytical tractability. Traffic hysteresis associated with transition between uncongested and congested states or between different equilibrium states is deferred to a future study. Second, we adopted the vertical measurement window for simplicity due to the lack of knowledge on the wave propagation in AV traffic. A better understanding of this feature may lead to a better selection of the measurement window. Third, for the purpose of analytical derivation, we made several simplifying assumptions such as homogeneous AV traffic and time-invariant and deterministic car-following features (i.e., constant parameters). However, the intrinsic stochastic nature of traffic flow can significantly impact traffic properties such as stability and capacity. Therefore, the deterministic assumption should be relaxed in the future. This can be achieved, for example, by embracing stochastic and time-varying CF models (e.g., Jiang et al., 2023). Further, linearization was undertaken to establish an analytical linkage between a CF law and dynamic FD. For enhanced precision, future research may address the nonlinear characteristics in CF laws by replacing the transfer function with data-derive functions, as demonstrated by prior works (e.g., Li & Ouyang, 2011; Zhou et al., 2023). Lastly, this study can also be extended to mixed traffic consisting of both AVs and human-driven vehicles to unveil how dynamic traffic features, as represented by dynamic FD, would evolve as the AV market penetration increases in the future.

Appendix A. Derivation of spacing

From Eqs. (7) and (8), we obtain:

$$x_0(t) = v_e t + \lim_{M\to\infty} \sum_{m=1}^{M} A_0^{(m)} \sin(\omega_m t + \phi_m), \tag{A.1}$$

$$x_N(t) = v_e t - N\Delta x_e + \lim_{M\to\infty} \sum_{m=1}^{M} A_0^{(m)} |G(j\omega_m)|^N \sin\big(\omega_m t + \phi_m + N\measuredangle G(j\omega_m)\big). \tag{A.2}$$

Therefore,

$$\begin{aligned} x_0(t) - x_N(t) &= N\Delta x_e + \sum_{m=1}^{M} A_0^{(m)} \big[\sin(\omega_m t + \phi_m) - |G(j\omega_m)|^N \sin\big(\omega_m t + \phi_m + N\measuredangle G(j\omega_m)\big)\big] \\ &= N\Delta x_e + \sum_{m=1}^{M} A_0^{(m)} \Big\{\Big[\Big(1 - |G(j\omega_m)|^N \cos\big(N\measuredangle G(j\omega_m)\big)\Big) \boldsymbol{\sin(\omega_m t + \phi_m)}\Big] - |G(j\omega_m)|^N \sin\big(N\measuredangle G(j\omega_m)\big) \boldsymbol{\cos(\omega_m t + \phi_m)}\Big\} \end{aligned} \tag{A.3}$$

For further simplification, assume $f(t) = \sum_{m=1}^{M} A_0^{(m)} \{[(1 - |G(j\omega_m)|^N \cos(N\measuredangle G(j\omega_m))) \boldsymbol{\sin(\omega_m t + \phi_m)}] - |G(j\omega_m)|^N \sin(N\measuredangle G(j\omega_m)) \boldsymbol{\cos(\omega_m t + \phi_m)}\} = C_1 \boldsymbol{\sin(\omega_m t + \phi_m)} - C_2 \boldsymbol{\cos(\omega_m t + \phi_m)}$.

According to trigonometry,

$$f(t) = C_1 \sin(\omega_m t + \phi_m) - C_2 \cos(\omega_m t + \phi_m) = R \sin(\omega_m t + \phi_m - \phi_c), \tag{A.4}$$

where the amplitude

$$R = \sqrt{(C_1)^2 + (C_2)^2} = \sqrt{\left(1 - |G(j\omega_m)|^N \cos(N\measuredangle G(j\omega_m))\right)^2 + \left(|G(j\omega_m)|^N \sin(N\measuredangle G(j\omega_m))\right)^2} = \sqrt{1 - 2|G(j\omega_m)|^N cos(N\measuredangle G(j\omega_m)) + |G(j\omega_m)|^{2N}}, \tag{A.5}$$

$$\phi_c = \arctan\frac{C_2}{C_1} = \arctan\frac{|G(j\omega_m)|^N \sin(N\measuredangle G(j\omega_m))}{1 - |G(j\omega_m)|^N \cos(N\measuredangle G(j\omega_m))}. \tag{A.6}$$

Therefore, we can have Equation (9).

Appendix B. Human driven vehicle vs. commercial AV

To apply our framework on human driven vehicles, we select the generalized linear optimal velocity model (GL-OVM). This model, extensively employed by researchers for its capability to emulate traffic flow, adopts a car-following structure represented as follows:

$$a_l(t) = \dot{v}_l(t) = \kappa[V(\Delta x_l(t)) - v_l(t)] \tag{A.7}$$

where $V(\Delta x_l(t))$ is the optimal speed function related to the spacing $\Delta x_l(t)$, κ is the sensitivity parameter. Then, the exponential optimal speed function established by Newell (1961) is denoted as:

$$V(\Delta x_l(t)) = v_0 \left[1 - \exp\left(-\frac{\alpha}{v_0}(\Delta x_l(t) - s_0)\right)\right] \tag{A.8}$$

where v_0 is the free-flow speed, s_0 is the jam distance, and α is the parameter related to the congested wave speed. Define $\hat{v}_l(t) := v_l(t) - v_e$ and $\Delta\hat{x}_l(t) := \Delta x_l(t) - \Delta x_e$, where $\hat{v}_l(t)$ is speed deviation from equilibrium speed v_e , $\Delta\hat{x}_l(t)$ is the spacing deviation from equilibrium spacing Δx_e.

Then, we linearize the CF law for human driven vehicles in Eq. (A.7) via Taylor expansion around the equilibrium state, in which $a_l(t) = 0$,

$$V(\Delta x_l(t)) = V(\Delta x_e) + \frac{V'(\Delta x_e)}{1!}(\Delta x_l(t) - \Delta x_e) \tag{A.9}$$

As $V(\Delta x_e)$ is the equilibrium speed, i.e., $V(\Delta x_e) = v_e = v_0 \left[1 - \exp\left(-\frac{\alpha}{v_0}(\Delta x_l(t) - s_0)\right)\right]$ according to Eq. (A.7). Eq. (A.9) can be further written as:

$$V(\Delta x_l(t)) = V'(\Delta x_e)(\Delta x_l(t) - \Delta x_e) + v_e \tag{A.10}$$

Substitute Eq. (A.10) into Eq. (A.7),

$$a_l(t) = \dot{v}_l(t) = \kappa[V'(\Delta x_e)(\Delta x_l(t) - \Delta x_e) + v_e - v_l(t)] \tag{A.11}$$

where $V'(\Delta x_e)$ is the first order derivative of optimal speed function in Eq. (A.7) with respect to the equilibrium spacing. It can be computed as:

$$V'(\Delta x_e) = \alpha \exp\left[-\frac{\alpha}{v_0}(\Delta x_e(v_e) - s_0)\right] \tag{A.12}$$

where $\Delta x_e(v_e)$ is the equilibrium spacing as a function of equilibrium speed v_e. Combining with Eq. (A.8) and solving for Δx_e when $v_l(t) = v_e$, we obtain

$$\Delta x_e(v_e) = s_0 - \frac{v_0}{\alpha}\ln\left(1 - \frac{v_e}{v_0}\right) \tag{A.13}$$

Plugging $\Delta\hat{x}_l$ and $\hat{v}_l(t)$ into Eq. (A.11), we have

$$\dot{\hat{v}}_l(t) = \kappa V'(\Delta x_e)\Delta\hat{x}_l(t) - \kappa\hat{v}_l(t) \tag{A.14}$$

Then we conduct Laplace transform to convert $\hat{v}_l$ and $\Delta\hat{x}_l$ into the frequency domain:

$$\Delta\hat{x}_l(s) = \frac{\hat{v}_{l-1}(s) - \hat{v}_l(s)}{s} \tag{A.15}$$

Finally, the transfer function of linearized OVM based on first order Taylor derivative $G_I(s)$ can be expressed as:

$$G_I(s) = \frac{\kappa V'(\Delta x_e)}{s^2 + \kappa s + \kappa V'(\Delta x_e)} \tag{A.16}$$

We further conduct a numerical experiment to compare the features of traffic hysteresis between human driven vehicles and AVs. For the parameter setting, we adopt the calibration results of OVM by Wang et al. (2012), where $v_0 = 33.3m/s$, $\kappa = 0.700s^{-1}$, $\alpha = 0.999s^{-1}$, and $s_0 = 1.62m$. For the linear controller, we use the calibration results for a commercial AV by Jiang et al. (2023), where $k_s = 0.3790\ (s^{-2})$, $k_v = 0.3937(s^{-1})$, $\tau = 0.8\ s, s_0 = 7.3625m$, and $\theta = 0sec$. Note that here $v_e = 25m/s$ and $A_0 = 10m$. Figure A1 shows the dynamic FD of GL-OVM and commercial AV respectively.

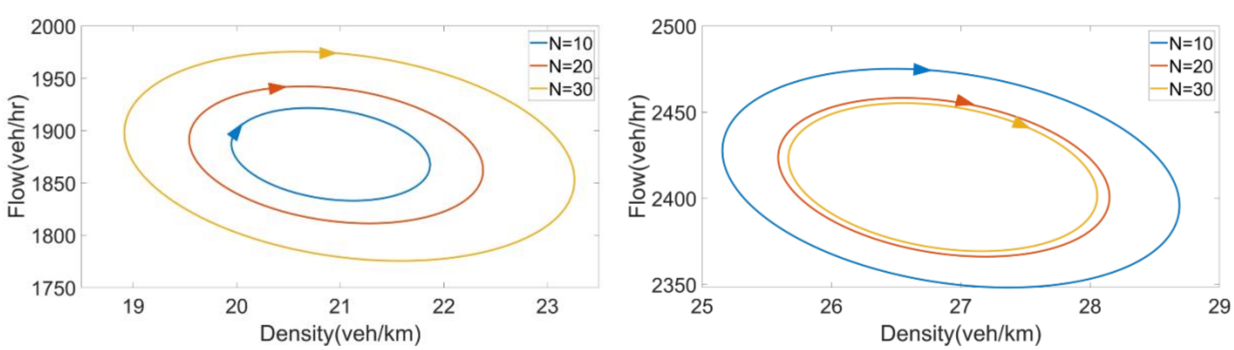

(a) (b)

Figure A1: CA Dynamic FD with different N: (a) GL-OVM and (b) commercial AV

From the figure, we can notice that though all hysteresis loops are clockwise for both models. However, the AV exhibits higher throughput and is string stable under the given oscillation setting, whereas a platoon based on GL-OVM is string unstable.

Acknowledgement

This work is supported by the U.S. National Science Foundation (Award CMMI 2129765).

References

Ahn, S., Cassidy, M. J., & Laval, J. (2004). Verification of a simplified car-following theory. *Transportation Research Part B: Methodological*, *38*(5), 431–440. https://doi.org/10.1016/S0191-2615(03)00074-2

Ahn, S., & Vadlamani, S. (2010). *Driver characteristics and their impact on traffic hysteresis and stop-and-go oscillations*. 1–25.

Ahn, S., Vadlamani, S., & Laval, J. (2013). A method to account for non-steady state conditions in measuring traffic hysteresis. *Transportation Research Part C: Emerging Technologies*, *34*, 138–147. https://doi.org/10.1016/j.trc.2011.05.020

Aw, A., & Rascle, M. (2000). Resurrection of "Second Order" Models of Traffic Flow. *SIAM Journal on Applied Mathematics*, *60*(3), 916–938. https://doi.org/10.1137/S0036139997332099

Carlson, R. C., Papamichail, I., Papageorgiou, M., & Messmer, A. (2010). Optimal Motorway Traffic Flow Control Involving Variable Speed Limits and Ramp Metering. *Transportation Science*, *44*(2), 238–253. https://doi.org/10.1287/trsc.1090.0314

Cassidy, M. J. (1998). Bivariate relations in nearly stationary highway traffic. *Transportation Research Part B: Methodological*, *32*(1), 49–59. https://doi.org/10.1016/S0191-2615(97)00012-X

Chen, D., & Ahn, S. (2015). Variable speed limit control for severe non-recurrent freeway bottlenecks. *Transportation Research Part C: Emerging Technologies*, *51*, 210–230.

Chen, D., Ahn, S., & Hegyi, A. (2014a). Variable speed limit control for steady and oscillatory queues at fixed freeway bottlenecks. *Transportation Research Part B: Methodological*, *70*, 340–358. https://doi.org/10.1016/j.trb.2014.08.006

Chen, D., Ahn, S., & Hegyi, A. (2014b). Variable speed limit control for steady and oscillatory queues at fixed freeway bottlenecks. *Transportation Research Part B: Methodological*, *70*, 340–358. https://doi.org/10.1016/j.trb.2014.08.006

Chen, D., Laval, J. A., Ahn, S., & Zheng, Z. (2012). Microscopic traffic hysteresis in traffic oscillations: A behavioral perspective. *Transportation Research Part B: Methodological*, *46*(10), 1440–1453. https://doi.org/10.1016/j.trb.2012.07.002

Coifman, B., Li, L., & Xiao, W. (2018). Resurrecting the Lost Vehicle Trajectories of Treiterer and Myers with New Insights into a Controversial Hysteresis. *Transportation Research Record: Journal of the Transportation Research Board*, *2672*(20), 25–38. https://doi.org/10.1177/0361198118786473

Edie, L. (1963). *Discussion of Traffic Stream Measurements and Definitions*. 139–154.

Greenshields, B. D., Bibbins, J. R., Channing, W., & Miller, H. H. (1935). *A study of traffic capacity*. *14*(1), 448–477.

Gunter, G., Gloudemans, D., Stern, R. E., McQuade, S., Bhadani, R., Bunting, M., Delle Monache,

M. L., Lysecky, R., Seibold, B., Sprinkle, J., Piccoli, B., & Work, D. B. (2021). Are Commercially Implemented Adaptive Cruise Control Systems String Stable? *IEEE Transactions on Intelligent Transportation Systems*, *22*(11), 6992–7003. https://doi.org/10.1109/TITS.2020.3000682

Gunter, G., Janssen, C., Barbour, W., Stern, R. E., & Work, D. B. (2020). Model-Based String Stability of Adaptive Cruise Control Systems Using Field Data. *IEEE Transactions on Intelligent Vehicles*, *5*(1), 90–99. https://doi.org/10.1109/TIV.2019.2955368

Han, Y., Chen, D., & Ahn, S. (2017). Variable speed limit control at fixed freeway bottlenecks using connected vehicles. *Transportation Research Part B: Methodological*, *98*, 113–134.

Han, Y., Hegyi, A., Zhang, L., He, Z., Chung, E., & Liu, P. (2022). A new reinforcement learning-based variable speed limit control approach to improve traffic efficiency against freeway jam waves. *Transportation Research Part C: Emerging Technologies*, *144*, 103900. https://doi.org/10.1016/j.trc.2022.103900

Hegyi, A., De Schutter, B., & Hellendoorn, J. (2005). Optimal coordination of variable speed limits to suppress shock waves. *IEEE Transactions on Intelligent Transportation Systems*, *6*(1), 102–112.

Jiang, J., Zhou, Y., Wang, X., & Ahn, S. (2023). *A Generic Stochastic Hybrid Car-following Model Based on Approximate Bayesian Computation*. https://doi.org/10.48550/ARXIV.2312.10042

Knoop, V. L., Duret, A., Buisson, C., & Van Arem, B. (2010). Lane distribution of traffic near merging zones influence of variable speed limits. *13th International IEEE Conference on Intelligent Transportation Systems*, 485–490. https://doi.org/10.1109/ITSC.2010.5625034

Kontar, W., Li, T., Srivastava, A., Zhou, Y., Chen, D., & Ahn, S. (2021). On multi-class automated vehicles: Car-following behavior and its implications for traffic dynamics. *Transportation Research Part C: Emerging Technologies*, *128*, 103166. https://doi.org/10.1016/j.trc.2021.103166

Laval, J. A. (2011). Hysteresis in traffic flow revisited: An improved measurement method. *Transportation Research Part B: Methodological*, *45*(2), 385–391.

Lebacque, J.-P., Mammar, S., & HajSalem, H. (2007). Generic second order traffic flow modelling. *Transportation and Traffic Theory 2007*, *Emerald*, 317–345.

Li, T., Chen, D., Zhou, H., Xie, Y., & Laval, J. (2022). Fundamental diagrams of commercial adaptive cruise control: Worldwide experimental evidence. *Transportation Research Part C: Emerging Technologies*, *134*, 103458. https://doi.org/10.1016/j.trc.2021.103458

Li, X., Cui, J., An, S., & Parsafard, M. (2014). Stop-and-go traffic analysis: Theoretical properties, environmental impacts and oscillation mitigation. *Transportation Research Part B: Methodological*, *70*, 319–339. https://doi.org/10.1016/j.trb.2014.09.014

Li, X., & Ouyang, Y. (2011). Characterization of Traffic Oscillation Propagation under Nonlinear Car-Following Laws. *Procedia - Social and Behavioral Sciences*, *17*, 663–682. https://doi.org/10.1016/j.sbspro.2011.04.538

Li, X., Wang, X., & Ouyang, Y. (2012). Prediction and field validation of traffic oscillation propagation under nonlinear car-following laws. *Transportation Research Part B: Methodological*, *46*(3), 409–423. https://doi.org/10.1016/j.trb.2011.11.003

Li, Z., Liu, P., Xu, C., Duan, H., & Wang, W. (2017). Reinforcement Learning-Based Variable Speed Limit Control Strategy to Reduce Traffic Congestion at Freeway Recurrent Bottlenecks. *IEEE Transactions on Intelligent Transportation Systems*, *18*(11), 3204–3217. https://doi.org/10.1109/TITS.2017.2687620

Logghe, S., & Immers, L. H. (2008). Multi-class kinematic wave theory of traffic flow. *Transportation Research Part B: Methodological*, *42*(6), 523–541. https://doi.org/10.1016/j.trb.2007.11.001

Makridis, M., Mattas, K., Anesiadou, A., & Ciuffo, B. (2021). OpenACC. An open database of car-following experiments to study the properties of commercial ACC systems. *Transportation Research Part C: Emerging Technologies*, *125*, 103047. https://doi.org/10.1016/j.trc.2021.103047

Nagel, K., & Nelson, P. (2005). *A critical comparison of the kinematic-wave model with observational data*. Transportation and Traffic Theory. Flow, Dynamics and Human Interaction. 16th International Symposium on Transportation and Traffic TheoryUniversity of Maryland, College Park.

Newell, G. F. (1993). A simplified theory of kinematic waves in highway traffic, part II: Queueing at freeway bottlenecks. *Transportation Research Part B: Methodological*, *27*(4), 289–303.

Papageorgiou, M., & Kotsialos, A. (2002). Freeway ramp metering: An overview. *IEEE Transactions on Intelligent Transportation Systems*, *3*(4), 271–281.

Papamichail, I., Kotsialos, A., Margonis, I., & Papageorgiou, M. (2010). Coordinated ramp metering for freeway networks–a model-predictive hierarchical control approach. *Transportation Research Part C: Emerging Technologies*, *18*(3), 311–331.

Payne, H. (1971). Models of freeway traffic and control. Mathematical models of public systems. Simulation councils. *Inc., Vista, CA, USA*.

Payne, H. J. (1971). Models of Freeway Traffic and Control. *In: Bekey, G.A., Ed., Mathematical Models of Public Systems, Simulation Council, La Jolla*, *1*, 51–61.

Shi, X., & Li, X. (2021). Constructing a fundamental diagram for traffic flow with automated vehicles: Methodology and demonstration. *Transportation Research Part B: Methodological*, *150*, 279–292. https://doi.org/10.1016/j.trb.2021.06.011

Smulders, S. A. (1986). Modelling and simulation of freeway traffic flow. *Department of Operations Research and System Theory [BS]*, *R 8615*.

Treiterer, J., & Myers, J. (1974). The hysteresis phenomenon in traffic flow. *Transportation and Traffic Theory*, *6*, 13–38.

Van Arem, B., Van Driel, C. J. G., & Visser, R. (2006). The Impact of Cooperative Adaptive Cruise Control on Traffic-Flow Characteristics. *IEEE Transactions on Intelligent Transportation Systems*, *7*(4), 429–436. https://doi.org/10.1109/TITS.2006.884615

Van Wageningen-Kessels, F., Van Lint, H., Vuik, K., & Hoogendoorn, S. (2015). Genealogy of traffic flow models. *EURO Journal on Transportation and Logistics*, *4*(4), 445–473. https://doi.org/10.1007/s13676-014-0045-5

Wang, M. (2018). Infrastructure assisted adaptive driving to stabilise heterogeneous vehicle strings. *Transportation Research Part C: Emerging Technologies*, *91*, 276–295. https://doi.org/10.1016/j.trc.2018.04.010

Wang, Y., Li, X., Tian, J., & Jiang, R. (2020). Stability Analysis of Stochastic Linear Car-Following Models. *Transportation Science*, *54*(1), 274–297. https://doi.org/10.1287/trsc.2019.0932

Wu, N. (2002). A new approach for modeling of Fundamental Diagrams. *Transportation Research Part A: Policy and Practice*, *36*(10), 867–884. https://doi.org/10.1016/S0965-8564(01)00043-X

Yao, Z., Gu, Q., Jiang, Y., & Ran, B. (2022). Fundamental diagram and stability of mixed traffic flow considering platoon size and intensity of connected automated vehicles. *Physica A:*

Statistical Mechanics and Its Applications, *604*, 127857. https://doi.org/10.1016/j.physa.2022.127857

Zhang, H. M. (1999). A mathematical theory of traffic hysteresis. *Transportation Research Part B: Methodological*, *33*(1), 1–23.

Zhang, H. M., & Kim, T. (2005). A car-following theory for multiphase vehicular traffic flow. *Transportation Research Part B: Methodological*, *39*(5), 385–399.

Zhou, J., & Zhu, F. (2020). Modeling the fundamental diagram of mixed human-driven and connected automated vehicles. *Transportation Research Part C: Emerging Technologies*, *115*, 102614. https://doi.org/10.1016/j.trc.2020.102614

Zhou, Y., Ahn, S., Wang, M., & Hoogendoorn, S. (2020). Stabilizing mixed vehicular platoons with connected automated vehicles: An H-infinity approach. *Transportation Research Part B: Methodological*, *132*, 152–170. https://doi.org/10.1016/j.trb.2019.06.005

Zhou, Y., Zhong, X., Chen, Q., Ahn, S., Jiang, J., & Jafarsalehi, G. (2023). Data-driven analysis for disturbance amplification in car-following behavior of automated vehicles. *Transportation Research Part B: Methodological*, *174*, 102768. https://doi.org/10.1016/j.trb.2023.05.005